Proton sheet crossing in thin relativistic plasma irradiated by a femtosecond petawatt laser pulse

Zheng Gong,[1] Yinren Shou,[1] Yuhui Tang,[1] Ronghao Hu,[2] Jinqing Yu,[3] Wenjun Ma,[1] Chen Lin,[1] and Xueqing Yan[1,4,*]

[1]*State Key Laboratory of Nuclear Physics and Technology, KLHEDP, and CAPT, School of Physics, Peking University, Beijing 100871, China*

[2]*College of Physics, Sichuan University, Chengdu 610065, China*

[3]*School of Physics and Electronics, Hunan University, Changsha 410082, China*

[4]*Collaborative Innovation Center of Extreme Optics, Shanxi University, Taiyuan, Shanxi 030006, China*

(Received 23 February 2020; accepted 9 June 2020; published 14 July 2020)

Leveraging on analyses of Hamiltonian dynamics to examine the ion motion, we explicitly demonstrate that the proton sheet crossing and plateau-type energy spectrum are two intrinsic features of the effectively accelerated proton beams driven by a drift quasistatic longitudinal electric field. Via two-dimensional particle-in-cell simulations, we show the emergence of proton sheet crossing in a relativistically transparent plasma foil irradiated by a linearly polarized short pulse with the power of one petawatt. Instead of successively blowing the whole foil forward, the incident laser pulse readily penetrates through the plasma bulk, where the proton sheet crossing takes place and the merged self-generated longitudinal electric field traps and reflects the protons to yield a group of protons with plateau-type energy spectrum.

DOI: 10.1103/PhysRevE.102.013207

I. INTRODUCTION

The energetic proton beam driven by highly intense laser pulse is regarded as a promising replacement for the conventional proton accelerators [1–3]. The potential advantages of laser-driven proton beams include but are not limited to high brilliance, low emittance, and ultrashot temporal duration [4,5], which are broadly pursued in scientific research, like fast ignition of confinement fusion [6–8], production of warm dense matter [9,10], proton radiography [11], and biomedical applications [12].

Recently, with the booming progress of high-intensity laser technology [13,14], various mechanisms were proposed to optimize the proton beam quality. Based on the distinct acceleration processes, the main mechanisms are divided into categories as target normal sheath acceleration (TNSA) [15–17], hole boring process [18–23], light sail radiation pressure acceleration (LS RPA) [24–31], shock wave acceleration [32–34], breakout afterburn (BOA) mechanism [35,36], magnetic vortex acceleration [37,38], and coulomb explosion (CE) [39,40]. Besides, several other schemes, like tailored target configuration [41,42], manipulation of chirped pulses [43,44], and acceleration assisted by external fields [45,46], also show the incremental effect in proton energy or beam collimation.

Among all these acceleration mechanisms, the LS RPA mechanism is favorable for its energy scaling law where the maximum accessible proton energy $\varepsilon_p^{\max}$ is nearly proportional to the quadratic of laser field amplitude a_0 [31,47]. Here, $a_0 = 0.85(I_0[10^{18}\mathrm{W/cm^2}]\lambda_0^2[\mu\mathrm{m}])^{1/2}$ is the normalized field strength and I_0 (λ_0) is the laser intensity (wavelength). For LS regime, an ultrathin foil plasma target is expected to be coherently accelerated as a whole. To avoid the broken of thin target caused by the $\mathbf{J}\times\mathbf{B}$ heating [48], circularly polarized (CP) laser pulses are generally employed in LS RPA to eliminate the electron sweeping oscillation in longitudinal direction. Near the optimal condition of $a_0 \sim \zeta$, monoenergetic ion beams with energy up to GeVs per nucleon can be achieved in multidimensional particle-in-cell (PIC) simulations [24,29,49]. In the above relation, $\zeta \equiv \pi(n_e/n_c)(l/\lambda_0)$ is the area density of the thin foil, where $n_c = (\omega_0^2 m_e)/(4\pi|e|^2) = 1.1\times10^{21}\mathrm{cm^{-3}}/(\lambda_0^2[\mu\mathrm{m}])^2$ is the critical density for laser with frequency ω_0, and l is the foil thickness. When the target thickness l becomes less than the plasma skin depth $l_s = c/\omega_{pe}$ ($\omega_{pe}^2 = 4\pi n_e|e|^2/m_e$) in which electrons are accelerated by the transmitted laser field, the LS RPA will evolve into a partially transparent "leaky" regime [50]. By comparison, when electrons are significantly heated by a linearly polarized (LP) pulse with duration of hundreds of femtosecond, an initially solid-density thin foil would undergo BOA process in the relativistic transparency regime [36]. Besides, it is worth emphasizing that the inevitable practical issues involved in laser-foil interaction such as preplasma [51–54] and kinetic instabilities [55,56] might modify the ion acceleration efficiency.

In experiment, the current record of laser-driven proton acceleration manifests a pronounced signal measured on 94 MeV [57], where the ultrathin foil is irradiated by a p-polarized pulse with intensity $\sim10^{20}\,\mathrm{W/cm^2}$ and duration $\sim$0.9 ps in a relativistic transparency regime, in which the the spatial distribution of the accelerated proton beams can be controlled by adjusting laser polarization [58] as well. This hybrid scheme combining the RPA and sheath acceleration dramatically enhances the proton energies [57], which could bridge the gap from the present accessible 94 MeV to potential 200 MeV prioritized by tumor treatment under the state-of-the-art petawatt laser facilities. Therefore, a deep understanding of interaction mechanism in relativistic transparency regime driven by LP pulses may facilitate this

*Electronic address: x.yan@pku.edu.cn

breakthrough. As is known to all, theoretically $\zeta \sim a_0$ is the optimal condition for achieving LS RPA for a CP laser pulse. However, in experiment, compared with the realization of RPA by utilizing CP pulse [59–63], ion acceleration driven by LP pulses exhibits more fruitful physical properties [64–70] and tends to be more reproducible to achieve protons with energy beyond half a hundred MeV [3,57,71–73]. Considering that the theoretical investigation of LP laser-driven ion acceleration near condition of $\zeta \sim a_0$ is seldom performed compared with the CP ones, we concentrate on examining how the LP laser pulse drive the proton acceleration under the condition of $\zeta \sim a_0$.

In this work, utilizing the analysis of Hamiltonian dynamics to examine the ion motion in a drifting quasistatic longitudinal electric field, we illustrate that the proton sheet crossing and plateau-type energy spectrum are two intrinsic features of the boosted proton bunch. By performing two-dimensional PIC simulations, we confirm the existence of proton sheet crossing when a LP laser pulse effectively heats the electrons to sustain a relativistically induced transparent plasma under the optimal parameter condition of LS RPA regime, i.e., $a_0 \sim \zeta$. It is worth emphasizing that, as far as we know, the phenomenon of proton sheet crossing has never been discussed before. Here, the pulse with a duration of 30 fs is one order of magnitude smaller than that utilized in BOA mechanism. In our scenario, instead of successively plowing the whole foil moving forward, the incident pulse readily penetrates through the plasma bulk and a large fraction of its energy is converted to hot electrons. When the foil is being irradiated by the pulse, the charged separated electric field at the front surface of target is swiftly merged with the the normal sheath field at the rear surface. The merged drifting quasistatic longitudinal electric field (QSLEF) possesses a ramp up profile which leads to the sheet crossing evolution of protons in the longitudinal direction. Another way of explaining sheet crossing is that the protons originally at the front surface overpassing the ones initially at the rear surface. The energy of protons become saturated after experiencing sheet crossing. Resorting to the theoretical analyses and PIC simulations, we clearly clarify how the protons are accelerated in the merged drifting QSLEF and why the sheet crossing takes place.

The manuscript consists of five sections as arranged below. In Sec. II, we theoretically investigate the ion acceleration induced by the subluminal drifting electric field via utilizing the analyses of hamiltonian dynamics. In Sec. III, we illustrate that the interaction between a short strong pulse and thin foil solid target takes place in a relativistically transparent regime by performing two-dimensional fully self-consistent particle-in-cell (PIC) simulations. In Sec. IV, we present the detailed processes such as proton acceleration and hot electron generation accompanying with the laser pulse penetrating through the transparent plasma. Finally, in Sec. V, we discuss the significance of this new proposed phenomenon in relevant practical applications and summarize our results.

II. THEORETICAL MODEL

In laser-driven ion acceleration, the source of the ion energy mainly comes from the QSLEF which is sustained by the accumulation of longitudinal charge separation in plasma induced by the incident strong pulse. Moreover, this QSLEF is gradually moving into the plasma target with the laser penetrating process. For simplicity, we consider the one-dimensional dynamics of ion acceleration in the moving frame of QSLEF. If the drifting velocity of QSLEF is assumed as constant v_d and the QSLEF does not explicitly depend on time t (i.e., $\partial E/\partial t = 0$), then the field strength can be described as $E(\xi)$ where $\xi = x - v_d t$ is the coordinate of ion in the moving frame of the drifting QSLEF. Given that the field amplitude is below the threshold of radiation dominant regime [74,75], we neglect the radiation reaction effect in analyses below. Consequently, the ion dynamics is characterized by the equations

$$\frac{dp}{dt} = |e|E(\xi), \tag{1}$$

$$\frac{d\xi}{dt} = \frac{p}{m_i\sqrt{1+(p/m_ic)^2}} - v_d. \tag{2}$$

Here the field velocity v_d is independent of time t, i.e., $dv_d/dt = 0$. The electric potential of QSLEF could be expressed as $\varphi(\xi) = -\int E(\xi)d\xi$, which is equivalent to $E(\xi) = -\partial\varphi(\xi)/\partial\xi$. Then the motion of an ion in the drifting QSLEF is determined by the conserved Hamiltonian

$$\mathcal{H}(\xi, p) = c\sqrt{m_i^2c^2 + p^2} - v_d p + \mathcal{Z}_i|e|\varphi(\xi). \tag{3}$$

Utilizing Hamiltonian dynamics to analyze the trapping and acceleration of charged particles can retrospect to exploration of nonlinear plasma wave [76]. Equations (1) and (2) of proton dynamics can be alternatively obtained through partial derivatives of Hamiltonian $dp/dt = -\partial\mathcal{H}(\xi, p)/\partial\xi$ and $d\xi/dt = \partial\mathcal{H}(\xi, p)/\partial p$. Via setting $dp/dt = 0$ and $d\xi/dt = 0$, we find a fixed point (ξ^*, p^*) in $\xi - p$ space, where the coordinate ξ^* satisfies the condition $E(\xi^*) = 0$ and $p^* = p_d = (v_d m_i)/\sqrt{1 - v_d^2/c^2}$ is equal to the momentum of mass m_i induced by the drifting velocity $v_d = (p_d/m_i)/\sqrt{1+(p_d/m_ic)^2}$. The fixed point describes a scenario that a kinetic ion with velocity v_d is co-moving with the drifting QSLEF and it never exchanges energy with the drifting electric field.

Considering that the plasma electrons and ions are partially separated and the entire net charge of the space is zero under one-dimensional circumstance, we come up with a practical situation of $E(\xi)$ having a single saw tooth profile, which is broadly adopted in previous theoretical models of laser-driven ion acceleration [25,28], to examine how the ions evolve to gain energy in the QSLEF. The electric field can be described as

$$E(\xi) = \begin{cases} 0, & \text{if } \xi \leqslant \xi_0, \\ E_0(\xi - \xi_0)/(\xi_1 - \xi_0), & \text{if } \xi_0 < \xi \leqslant \xi_1, \\ -E_0(\xi - \xi_2)/(\xi_2 - \xi_1), & \text{if } \xi_1 < \xi \leqslant \xi_2, \\ 0, & \text{if } \xi_2 < \xi, \end{cases} \tag{4}$$

where E_0 is the peak amplitude of field strength. As a result, the electric potential is calculated via $\varphi(\xi) = \varphi(-\infty) -$

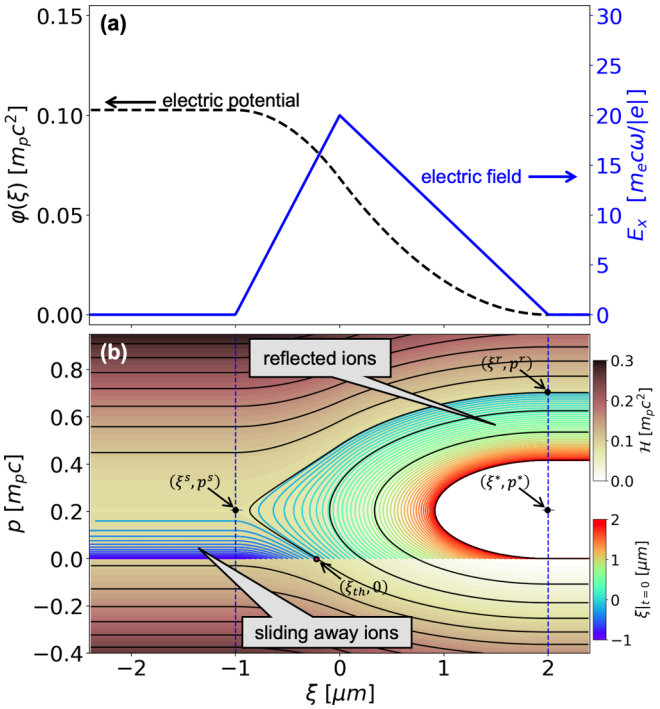

FIG. 1. The black dashed line represents the electric potential $\varphi(\xi)$ while the blue solid one illustrates the longitudinal electric field $E(\xi)$. (b) The background contour with brown color map renders the Hamiltonian value $\mathcal{H}(\xi, p)$ in the unit of proton rest energy m_pc^2 and the blue dashed lines denote the boundary of the electric field at $\xi = -1\ \mu$m and $2\ \mu$m. The lines with the rainbow colorcode exhibit the evolution of protons (originally locating at $-1 \leqslant \xi\ [\mu m] \leqslant 2$) in $\xi - p$ phase space. Panels (a) and (b) share the same horizontal axis.

$\int_{-\infty}^{\xi} E(\xi)d\xi$ as

$$\varphi(\xi) = \begin{cases} E_0\frac{\xi_2-\xi_0}{2}, & \text{if } \xi \leqslant \xi_0, \\ E_0\frac{\xi_2-\xi_0}{2} - E_0\frac{(\xi-\xi_0)^2}{2(\xi_1-\xi_0)}, & \text{if } \xi_0 < \xi \leqslant \xi_1, \\ E_0\frac{(\xi-\xi_2)^2}{2(\xi_2-\xi_1)}, & \text{if } \xi_1 < \xi \leqslant \xi_2, \\ 0. & \text{if } \xi_2 < \xi. \end{cases} \tag{5}$$

Here the potential at the $\xi \leqslant \xi_0$ is set as $\varphi(\xi) = E_0(\xi_2 - \xi_0)/2$ and thus the downstream potential at $\xi \geqslant \xi_2$ is $\varphi(\xi) = 0$. Without losing generality, the relevant parameters can be set as: $\xi_0 = -1\ \mu$m, $\xi_1 = 0\ \mu$m, $\xi_2 = 2\ \mu$m, $E_0 = 20m_ec\omega_0/|e|$, $\beta_d = v_d/c = 0.2$, $\mathcal{Z}_i = 1$, and $m_i = m_p = 1836m_e$. Therefore, the maximum electric potential is approximated as $|e|\varphi(\xi_0)/(m_pc^2) \approx 0.103$, where $\omega_0 = 2\pi c/\lambda_0$ is in accordance with $\lambda_0 = 1\ \mu$m. It is worth pointing out that the above values being chosen is because that these parameters represent the typical characteristics of the drift QSLEF in the realistic scenario of PIC simulations.

The profile of QSLEF $E(\xi)$ and potential $\varphi(\xi)$ are illustrated in upper panel of Fig. 1. The distribution of Hamiltonian $\mathcal{H}(\xi, p)$ is shown in the lower panel of Fig. 1, where the evolution of initial static protons at $-1 \leqslant \xi|_{t=0}\ [\mu m] \leqslant 2$ is plotted as well. The trajectories of protons in $\xi - p$ space demonstrate that there are two typical groups of protons absorbing energy from the QSLEF and there is a threshold of initial position $\xi = \xi_{\rm th}$ to classify them. The first group, whose original position is $\xi|_{t=0} < \xi_{\rm th}$, at the initial stage do not obtain enough energy to catch up with the positive part of drifting QSLEF so that they are overtaken by the QSLEF and miss the opportunity of successively gaining energy to sustain a positive momentum. These protons are labeled as the *sliding away ions* in Fig. 1(b). The other ones with $\xi|_{t=0} > \xi_{\rm th}$ can be trapped by the potential well of Hamiltonian $\mathcal{H}(\xi, p)$ and subsequently be efficiently accelerated by the moving electric field. At the initial stage the protons are slower than the drifting electric field. Then, after absorbing energy from the QSELF, the proton has a velocity v greater than v_d and the acceleration time is substantially extended up to its surpassing the drifting QSELF. In the moving frame of QSLEF, the motion of these efficiently accelerated protons is analogous to be reflected by the potential well and therefore they are labeled as *reflected ions* in Fig. 1(b).

For the purpose of determining the threshold $\xi_{\rm th}$ of discriminating the above two acceleration regimes, we utilize the conservation relation of Hamiltonian $\mathcal{H}(\xi, p)$ between the separatrix points $(\xi^s, p^s) = (\xi_0, p_d)$ and threshold $(\xi_{\rm th}, 0)$. The resulting $\xi_{\rm th}$ satisfies

$$\frac{|e|\varphi(\xi_{\rm th})}{m_pc^2} + 1 = \frac{|e|\varphi(\xi_0)}{m_pc^2} + \frac{1}{\gamma_d}, \tag{6}$$

where $\gamma_d = 1/\sqrt{1-\beta_d^2}$ is the relativistic Lorentz factor of an object with dimensionless velocity β_d. Following the above parameter condition $|e|\varphi(\xi_0)/(m_pc^2) \approx 0.103$ and $\gamma_d \approx 1.0206$, we arrive at the threshold $\xi_{\rm th} \approx -0.23\ \mu$m.

When the initial position of a static proton $\xi|_{t=0}$ is a little larger than the threshold $\xi_{\rm th}$, i.e., $\xi|_{t=0} \to \xi_{\rm th}^+$, the proton is able to achieve the maximum energy from the QSELF. The maximum accessible energy of original static protons can be derived through the conservation of Hamiltonian $\mathcal{H}$ between points (ξ^s, p^s) and (ξ^r, p^r), where $\xi^s = \xi_0$, $p^s = p_d$, and $\xi^r = \xi_2$. Substituting these expressions into Eq. (3), we find the momentum of reflected proton p^r is incorporated in the quadratic equation

$$\left(1-\beta_d^2\right)\left(\frac{p^r}{m_pc}\right)^2 - 2\beta_d\mathcal{B}\left(\frac{p^r}{m_pc}\right) + 1 - \mathcal{B}^2 = 0, \tag{7}$$

where $\mathcal{B} = \frac{|e|\varphi(\xi_0)}{m_pc^2} + \frac{1}{\gamma_d}$ and the solutions are written as

$$\frac{p^{r\pm}}{m_pc} = \frac{\beta_d\mathcal{B} \pm \sqrt{\mathcal{B}^2 + \beta_d^2 - 1}}{1-\beta_d^2}. \tag{8}$$

It is obvious that p^{r+} is the maximum accessible momentum of protons reflected by the QSLEF. In contrast, p^{r-} denotes a initial condition of proton with $\varphi(\xi)|_{t=0} = 0$ to achieve the maximum energy gain during the reflection process. Taking the above parameters into Eq. (8), we get the maximum reflected momentum $p^{r+} \approx 0.705$ and cutoff proton energy $\varepsilon_p^{\rm cut} \approx 209$MeV, which is in good agreement with the energy spectrum in the inset of Fig. 2(a).

The protons experiencing the relatively stronger QSLEF would gradually get up with or even overtake the front protons exposed to the weaker QSLEF. The proton distribution in $x - p$ space is exhibited in Fig. 2(a), where protons' initial position is rendered in rainbow color map. In the laboratory

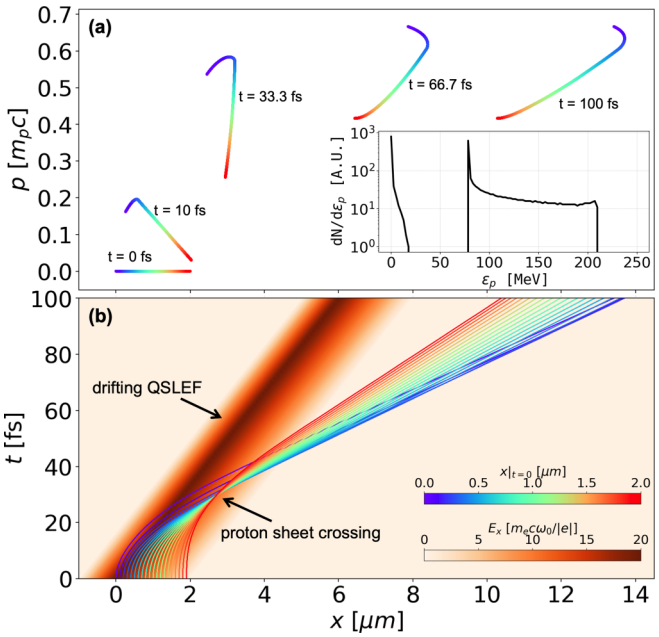

FIG. 2. The scattering distribution of protons in $x-p$ phase space, where the protons initially locating at $0 \leqslant \xi[\mu\mathrm{m}] \leqslant 2$ is coded by rainbow color map. The inset illustrates the proton energy spectrum at time $t = 100$ fs. (b) The trajectories of proton motion, where the background cool-warm color map renders the strength of drifting QSELF. Panels (a) and (b) share the same horizontal axis and rainbow color scale.

frame, the occurrence of overtaking becomes a trajectory intersection, termed as "sheet crossing" in breaking of nonlinear Langmuir wave, as shown in Fig. 2(b). Here, we emphasize that the two traits, plateau-type energy spectrum and sheet crossing of protons, are intrinsically incorporated in the mechanism of ion acceleration driven by drifting QSLEF, which is independent of the form of generation of QSLEF such as plasma wakefield [77,78], transparent hole-boring [79], electrostatic shocks [32,33,80,81] or dual-peaked electrostatic field [82].

Moreover, the criterion of sheet crossing occurrence of the reflected protons can be theoretically determined via the conserved Hamiltonian. This criterion can be understood as the existence of the solution ξ_{th} in Eq. (6), i.e., $|e|\varphi(\xi_0)/(m_pc^2) + 1/\gamma_d > 1$ which is equivalent to $p^{r-} < 0$ in Eq. (8). After some trivial algebra calculation, this criterion can be expressed as

$$\beta_d < \beta^* \equiv \sqrt{2\frac{|e|\varphi(\xi_0)}{m_pc^2} - \left[\frac{|e|\varphi(\xi_0)}{m_pc^2}\right]^2} \tag{9}$$

under the condition of $|e|\varphi(\xi_0)/m_pc^2 < 1$ which is always satisfied for the QSLEF driven by the state-of-the-art laser facility. To clearly illustrate the underlying physics of this criterion, two more simulations of the drift velocity β_d nearby the criterion β^* are carried out. After taking $|e|\varphi(\xi_0)/(m_pc^2) \approx 0.103$ into Eq. (9), the criterion is calculated as $\beta^* \approx 0.442$. As shown in Fig. 3(a) for $\beta_d = 0.45 > \beta^*$, none of the protons original from $-1 \leqslant \xi\ [\mu\mathrm{m}] \leqslant 2$ can obtain enough energy to catch up with the moving QSLEF and thus the their

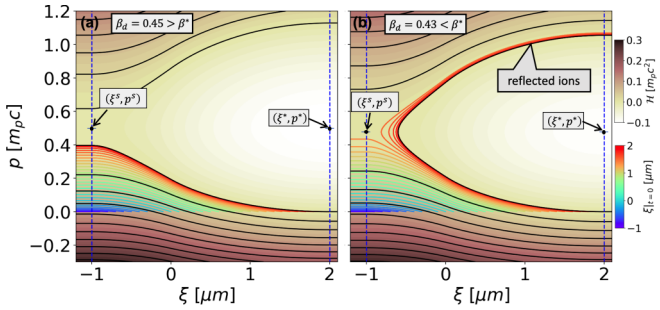

FIG. 3. The trajectories of proton in (ξ, p) space. All the parameters of the simulations are same as those in Fig. 1 except for the drift velocity being $\beta_d = 0.45$ in panel (a) and $\beta_d = 0.43$ in panel (b).

trajectories cannot intersect with each other along x direction. On the contrary, when $\beta_d < \beta^*$ as shown in Fig. 3(b), the protons with original position $\xi_{\mathrm{th}}\ [\mu\mathrm{m}] < \xi\ [\mu\mathrm{m}] \leqslant 2$ would be reflected by the drift QSLEF and the momentum of initial back protons is larger than that of initial front ones which would result in the occurrence of sheet crossing. In deriving the criterion of β^*, the condition of $p^{r-} < 0$ does not mean that the accelerated protons would have a negative longitudinal momentum. The $p^{r-} < 0$ is for the proton initial condition at $\varphi(\xi) = 0$ to achieve the maximum energy p^{r+}, and it can be understood as the criterion to switch on the reflected acceleration. In other words, if $p^{r-} < 0$, then there must be protons with $p|_{t=0} = 0 > p^{r-}$ to satisfy the criterion of reflected acceleration process. However, if $p^{r-} > 0$, then all the original static protons cannot be reflected by the drift electric field and thus all of them becomes the *"sliding away ions"* as shown in Fig. 3(a).

The dependence of β^* on $\varphi(\xi_0)$ in Eq. (9) indicates that once the electric potential $\varphi(\xi_0)$ of QSLEF is given, the corresponding maximum drifting velocity $\beta_d = \beta^*$ is determined. Taking $\partial p^{r+}/\partial\beta_d > 0$ into account, the maximum proton energy is monotonically increasing with the raise of β_d. Substituting $\varphi(\xi_0)$ and $\beta_d = \beta^*$ into Eq. (8), we can reach to $p^{r+}/m_pc = 2\sqrt{2\widetilde{\varphi} - \widetilde{\varphi}^2}/(1-\widetilde{\varphi})^2$, where $\widetilde{\varphi} = |e|\varphi(\xi_0)/m_pc^2$ is the normalized dimensionless electric potential. Utilizing $\gamma^{\max} = \sqrt{1 + (p^{r+}/m_pc)^2}$, the maximum achievable energy under a given $\widetilde{\varphi}$ can be derived as

$$\gamma^{\max} = \frac{4\widetilde{\varphi} - 2\widetilde{\varphi}^2}{(1-\widetilde{\varphi})^2}. \tag{10}$$

Here the $\gamma^{\max}$ only denotes the maximum achievable proton energy under the optimal condition $\beta_d \approx \beta^*$ for the fixed electric potential $\widetilde{\varphi} = |e|\varphi(\xi_0)/m_pc^2$ of the drift QSLEF and it does not guarantee the necessity of the optimal acceleration taking place.

III. KINETIC SIMULATION RESULTS

In this section, a series of two-dimensional simulations have been performed via relativistic fully self-consistent PIC code EPOCH [83]. The simulation domain is a rectangle of $80\lambda_0 \times 30\lambda_0$ being uniformly divided by cells with the same size of $1/100\lambda_0 \times 1/100\lambda_0$, where $\lambda_0 = 0.8\,\mu\mathrm{m}$ is laser wavelength. The incident pulse with linearly polarized field E_y has a Gaussian temporal profile with $\tau_0 = 30$ fs in

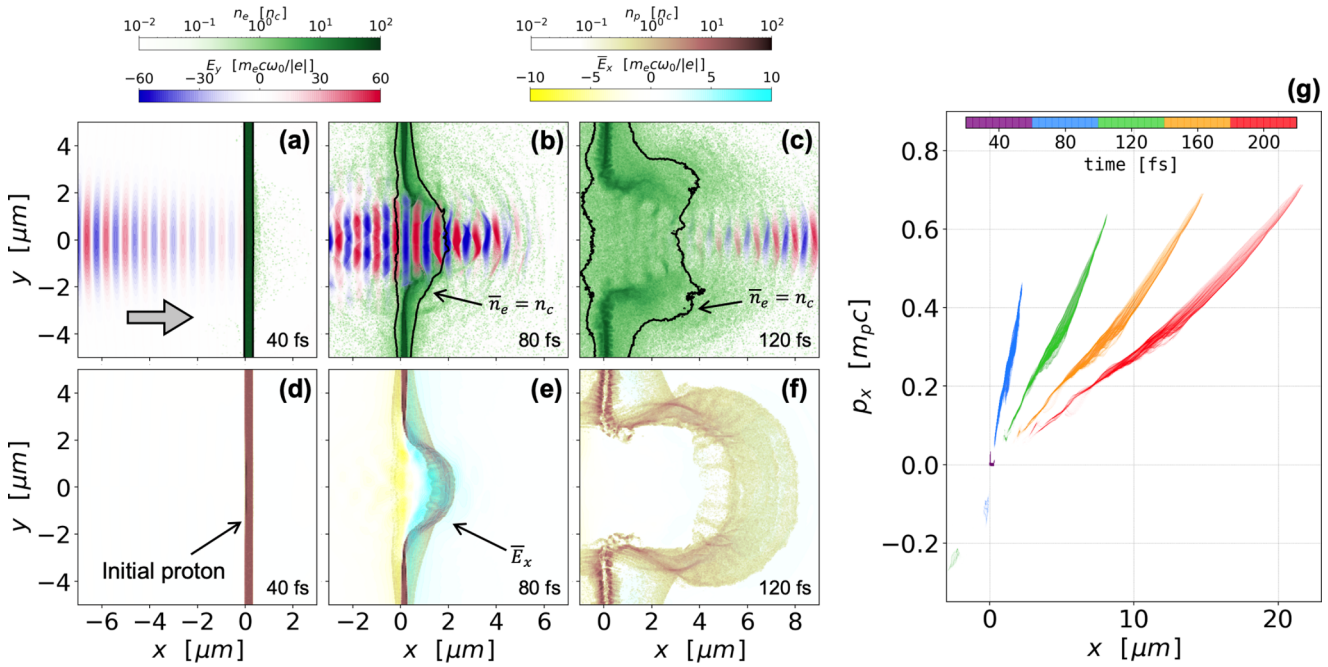

FIG. 4. The spatial distributions of the transverse electric field E_y and plasma electron density n_e are presented in panels (a, b, c) for different time snapshots. The gray arrow in panel (a) marks the propagation direction of the incident laser pulse. The black lines in panels (b, c) outline the interface of plasma critical density $\overline{n}_e = n_c$, where the overline denotes the value which is temporally averaged over four laser period. The spatial distributions of the time averaged longitudinal field $\overline{E}_x$ and proton density n_p are exhibited in panels (d, e, f), which corresponds to the same time as that in panels (a, b, c), respectively. The scattering plot of proton particles is illustrated in panel (g) where the colors represent the different time.

full-width-half-maximum (FWHM) of laser intensity. Its transverse spatial profile is Gaussian as well and the spot size is $\sigma_0 = 2\,\mu$m (in $1/e$ of field amplitude) at the point of focusing $x = 0\,\mu$m. The peak amplitude of the laser field is $a_0 = 61.2$ equivalent to the intensity $I_0 = 8 \times 10^{21}\,\mathrm{W/cm^2}$ and the power can be estimated as $P \approx 1$PW. The plastic thin target located at $0 < x\,[\mu\mathrm{m}] < 0.3$ consists of the polyethylene CH_2 material, where the plasma density is $n_e = 52n_c$, $n_p = 13n_c$, and $n_{\mathrm{carbon}} = 6.5n_c$ for electron, proton, and carbon, respectively. The initialization of loading macro-particles are 60 electrons, 40 protons, and 20 carbon ions per cell, respectively. The initial temperature is set as $T_e = 100$ keV for electron to resolve the Debey length and the ion temperature is set as $T_i = 1$ keV. Here, open boundary condition is adopted for both fields and particles.

Since the intensity of laser pulse is three orders of magnitude higher than the relativistic criterion $I_{\mathrm{re}} = 1.37 \times 10^{18}\,\mathrm{W/cm^2}\lambda_0\,[\mu\mathrm{m}]^{-2}$, the solid foil is able to be fully ionized by the rising part of laser field. Therefore, it is reasonable to treat the target as fully ionized plasma initially. The spatial distribution of electron density n_e and laser transverse electric field E_y are exhibited in Figs. 4(a), 4(b), and 4(c) for three snapshots. At time $t \approx 75$ fs, the peak amplitude of laser field reaches the front surface of the target ($x = 0\,\mu$m). The counterintuitive thing is that instead of boosting the whole target foil forward, the laser pulse readily penetrates through the overdense plasma as shown in Figs. 4(b) and 4(c), where the contour of critical density $\overline{n}_e = n_c$ manifests the expansion of plasma electron after the laser leaves away. The original opaque overdense plasma becomes transparent to the laser light, which is interpreted by the relativistic transparency mechanism [84], in which for a thick overcritical ($n_e > n_c$) plasma target, the cutoff plasma density for a laser pulse propagation is extended up to $\tilde{\gamma} n_c \approx a_0 n_c$ when electrons are heated to an effective energy $\tilde{\gamma} m_e c^2 \approx a_0 m_e c^2$ induced by the transverse oscillating laser field E_y.

The spatial distribution of proton density n_p and the longitudinal electric field $\overline{E}_x$ are exhibited in Figs. 4(d), 4(e), and 4(f), where the overline of $\overline{E}_x$ indicates that the value is time averaged over four laser periods. The self-generated longitudinal field $\overline{E}_x$, same as above QSLEF, is produced by the charge separation between the electrons and ions, whose maximum strength is close to 50 TV/m at $t = 80$ fs when the peak amplitude of laser pulse arrives at the rear surface of target. The protons nearby central region are pushed forward by the $\overline{E}_x$ as shown in Fig. 4(e). At the later time $t = 120$ fs, the strength of self-generated QSLEF $\overline{E}_x$ substantially declines when the laser pulse leaves from the area of classical overdense plasma. Meanwhile, the protons gradually terminate their acceleration and enter the free-floating state. The scatter distributions of protons in $x - p_x$ space are presented in Fig. 4(g) where the protons initially locate at $-2 \leqslant y\,[\mu\mathrm{m}] \leqslant 2$ are selected. At $t = 40$ fs protons are almost static when the rising part of laser field touches the front surface of target. Instead, however, the protons are immediately boosted to a energy around 90 MeV ($p_x \approx 0.45 m_p c$) at time $t = 80$ fs, and then they continuously absorb energy from the QSLEF $\overline{E}_x$ to achieve a cutoff energy $\varepsilon_p \approx 170$ MeV ($p_x \approx 0.63 m_p c$) at $t = 120$ fs. After that, the protons experience a relative weak acceleration by the decayed QSLEF and their eventual maximum energy approximates 210 MeV ($p_x \approx 0.63 m_p c$).

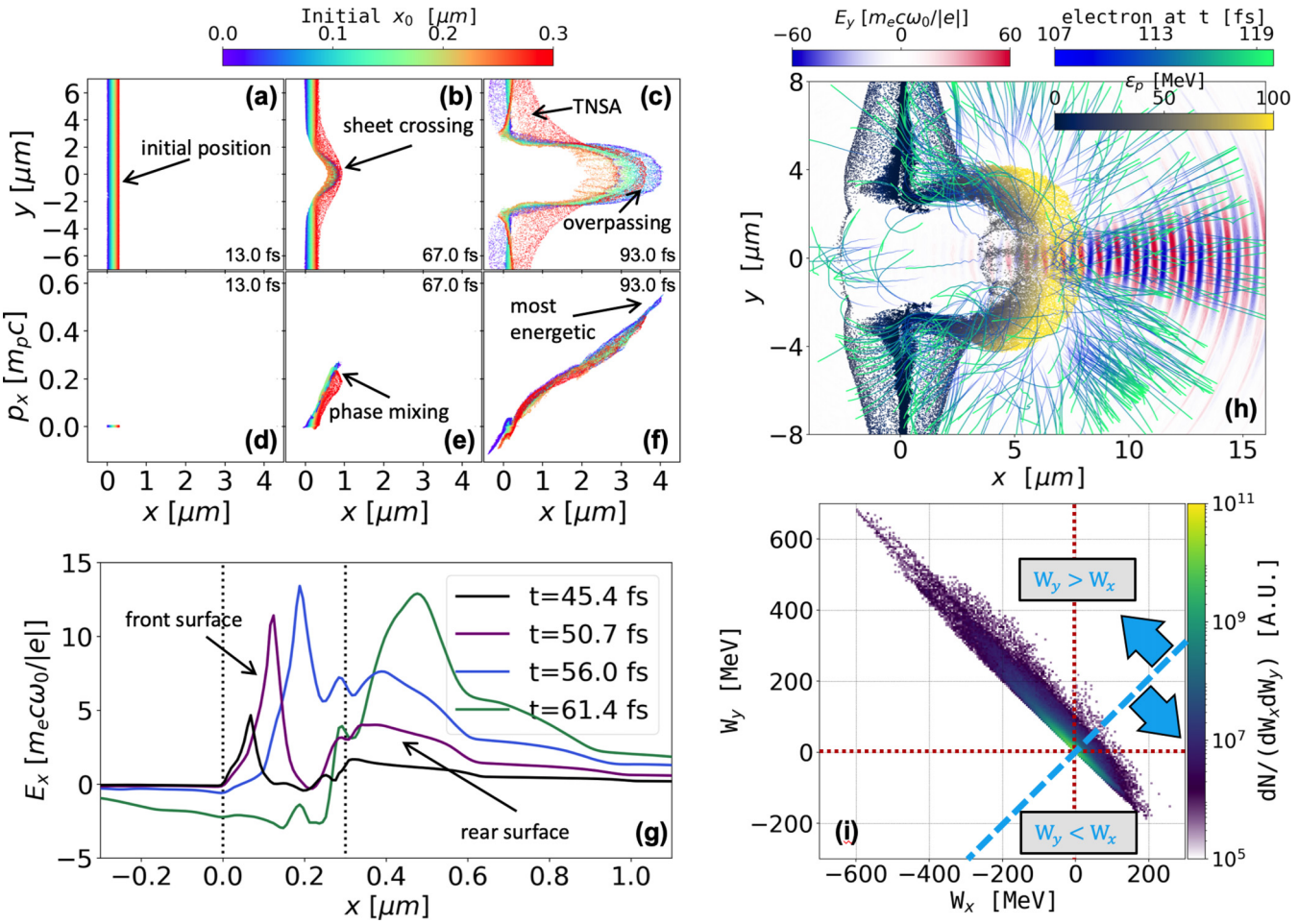

FIG. 5. Panels (a, b, c) show the distribution of protons with the color rendering their original position x_0, while panels (d, e, f) exhibit the proton distribution in $p_x - x$ phase space with the same color scheme. Panel (g) outlines the profile of longitudinal electric field E_x for four simulation time, where E_x is transversely averaged over $-2.5 \leqslant y\,[\mu\text{m}] \leqslant 2.5$ and the dotted black lines mark the target initial position. Panel (h) shows the evolution of typical electron trajectories (rendered in winter color map) during $107 < t < 120$ fs, where the distribution of proton particles and transverse electric field are presented as well. Panel (i) exhibits the electron energy contribution from transverse work W_y and longitudinal work W_x.

To understand how protons grab energy from the QSLEF $\overline{E}_x$, we pay attention to the interaction process during $40 < t\,[\text{fs}] < 120$. The protons' original position x_0 is coded in rainbow color scale as shown in Figs. 5(a) and 5(d). The interesting thing of proton sheet crossing is that near the central axis the protons original from front surface of target intersect with the those from rear surface in Fig. 5(b). The similar phenomenon of sheet crossing in area of laser wakefield acceleration [85], occurs in underdense plasma where the breaking of nonlinear Langmuir wave enables the self-injection of electrons into the favorable accelerating phase [86]. Another feature of proton dynamics is the phase mixing in $x - p_x$ phase space as shown in Fig. 5(e), where the ("blue") protons from front surface have mixed with ("red") ones from rear surface. This feature is different from the hybrid acceleration mechanism in a thick solid slab [32]. The longitudinal momentum of "blue" protons is larger than that of "red" protons at $t = 67$ fs in Fig. 5(e) implying the occurrence of overtaking later. In Fig. 5(c), the "blue" protons overpass the "red" proton in the central region whilst the peripheral proton is dominated by the sheath field acceleration. At $t = 93$ fs, the most energetic protons are those from the front target surface as exhibited in Fig. 5(f).

The longitudinal profile of QSLEF E_x is outlined in Fig. 5(g), where the E_x is spatially averaged with the extent of $-2 \leqslant y\,[\mu\text{m}] \leqslant 2$ along the transverse direction. At the beginning time, it is pronounced that the field at the front surface is much stronger than that at the rear surface. At $t = 50.7$ fs the peak of the front E_x attains $11.5(m_ec\omega_0/|e|)$ but the rear E_x is only up to $3.5(m_ec\omega_0/|e|)$, where $m_ec\omega_0/|e| \approx 4.4 \times 10^{12}$ V/m is equivalent to the field strength of $a_0 = 1$. As the accelerating field imposed on the front surface protons is stronger, the resulting energy chirp leads to the sheet crossing process. During $45 \leqslant t\,[\text{fs}] \leqslant 56$, the strength of field at front surface escalates as the electron populations in piled up charge separation is enhanced by the rising profile of incident laser intensity. Similarly, the strength of E_x at rear surface raises as well. Accompanying with the penetration of laser pulse through the thin foil, the front charge separation field is combined with the field at rear surface sustained by the expanded hot electrons at $t \approx 61$ fs.

TABLE I. Parameter setup for cases with different spot size.

σ_0 [μm]	a_0	n_e [n_c]	n_p [n_c]	n_{ca} [n_c]	ζ
1	122.4	104	26	13	122
2	61.2	52	13	6.5	61
4	30.6	26	6.5	3.25	31
8	15.3	13	3.25	1.625	15
12	10.2	8.7	2.17	1.085	10

The above simulations manifest that the energy increment of protons predominantly takes place before $t = 120$ fs. The trajectories of typical hot electrons in Fig. 5(h) demonstrate that energetic electrons disperse after the pulse completely gets rid of the plasma region (more detailed animation in the Supplemental Material [87]), where 5% of all the electrons with condition of $\varepsilon_e \geqslant 80$ MeV at 100 fs are chosen. Therefore, the source of the QSLEF is dissipated with the divergence of the accumulated electron sheath. As shown in the Supplemental Material animation [87], these electrons assemble in the central region to facilitate the proton acceleration during $50 \leqslant t$ [fs] $\leqslant 100$ and then immediately disperse after $t = 100$ fs. At 100 fs, the energy contribution of electrons from longitudinal or transverse work is exhibited in Fig. 5(i), where the dashed skyblue line marks the boundary of $W_y = W_x$. Here, $W_x = \int |e|E_x dx$ ($W_y = \int |e|E_y dy$) corresponds to work done by the longitudinal (transverse) electric field. From Fig. 5(i), we conclude that the electron energy are primarily from the work W_y done by the transverse electric field whilst the longitudinal work W_x mainly leads to the energy reduction. The reason of unfavorable contribution of W_x could be understood as that the positive QSLEF plays a decelerating role in negative charged electrons. Briefly, the interaction scenario becomes that the laser transfers its energy to electrons through the work W_y caused by transverse oscillating field and then the electrons convert their energy to protons via the work W_x induced by QSLEF.

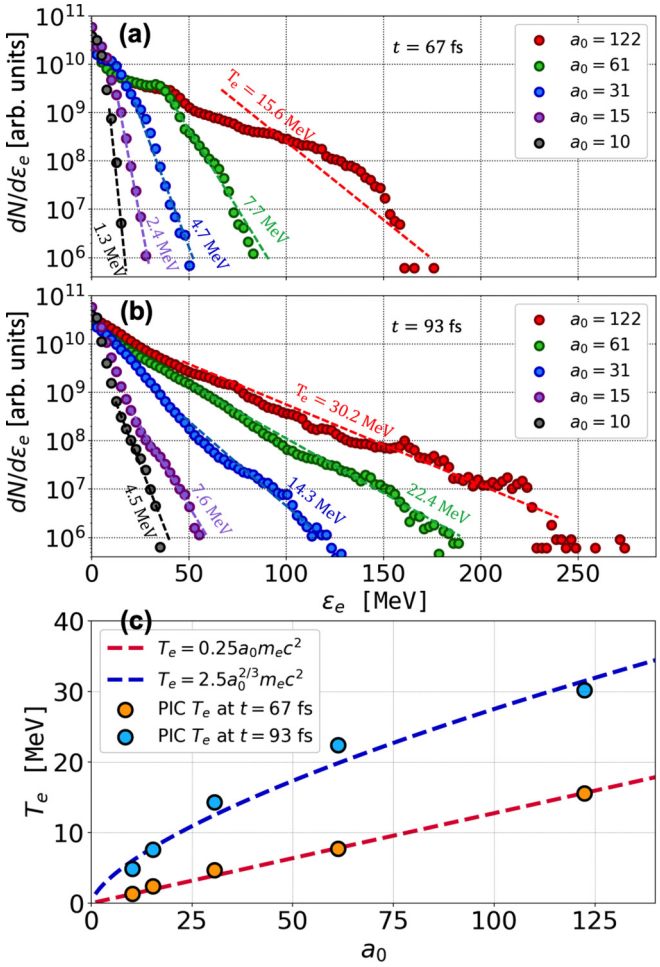

FIG. 6. Panel (a) exhibits electron energy spectral for different laser field amplitude a_0 at time $t = 67$ fs, where the reciprocal slope of dashed lines indicate the electron temperature. Panel (b) is same as panel (a) but for $t = 93$ fs. Panel (c) presents the dependence of electron temperature on laser intensity a_0.

IV. PROTON ACCELERATION AND HOT ELECTRON GENERATION

For the purpose of investigating the optimized combination of spot size σ_0 and intensity I_0 under a fixed power $P = 1$PW, we change the laser field amplitude a_0 by adjusting the spot size σ_0. Meanwhile, to keep $\zeta \sim a_0$, the plasma electron density is varied correspondingly. The detailed parameter setup is listed in Table I. It should be noticed that to avoid the leakage of the incident energy, the transverse size of the simulation domain is extended to $60\lambda_0$ and $90\lambda_0$ for the cases of the laser spot size equaling 8 μm and 12 μm.

As shown in Fig. 4, the relativistic transparency enables the laser pulse to pass through the overdense plasma region. This scenario is analogous with the laser propagating inside the underdense plasma, where the quasistatic transverse electric field and azimuthal magnetic field are ubiquitously sustained [88,89]. The existence of combined field indicates several potential acceleration mechanisms [90–95] would contribute to boost the electron energy. The electron energy spectral for different laser intensities at time $t = 67$ and 93 fs are shown in Figs. 6(a) and 6(b). The electron temperature of these two moments corresponds to the upper and lower boundary of electron temperature in the proton acceleration process. The moment $t = 67$ fs is the beginning of proton effective acceleration by combined charge separation field when the plasma target has not been completely broken. The later moment $t = 93$ fs is the ending of primary proton acceleration and after that the protons merely undergo a drifting motion with a little energy boost. The dependence of hot electron temperature on laser intensity a_0 is illustrated in Fig. 6(c), where the circle dots represent the results from two-dimensional (2D) PIC simulations while the dashed lines are fitting curves. At the early time 67 fs, the temperature of electrons is proportional to the laser field amplitude, i.e., $T_e \propto a_0$. In contrast, the electron energy is substantially enhanced and the scaling of electron temperature becomes $T_e \propto a_0^{2/3}$ later. For the case of $\sigma_0 = 2\,\mu$m and $a_0 = 61$, the electron temperature is multiplied by a factor of three from 7.7 to 22.4 MeV. Such a drastic variation in electron energy indicates the interaction in an unequilibrium state, which indicates the necessity of

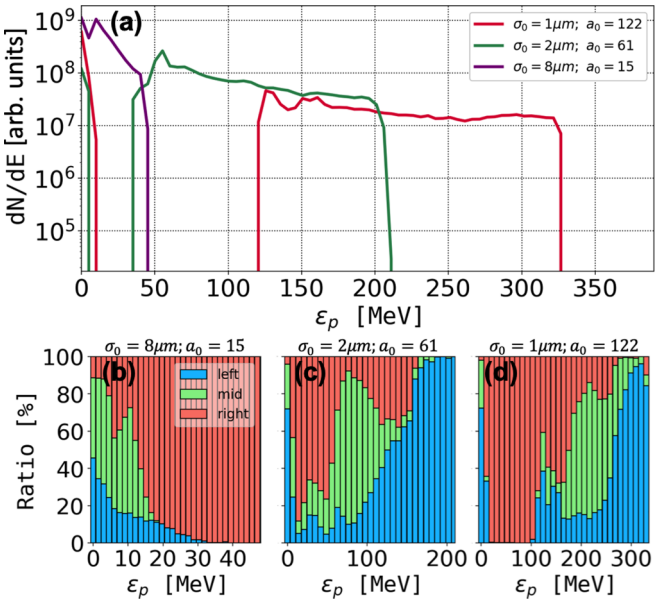

FIG. 7. Panel (a) plots the proton energy spectra for three cases. Panels (b–d) show the ratio of "left," "mid," and "right" proton occupation over the proton energy spectra, respectively.

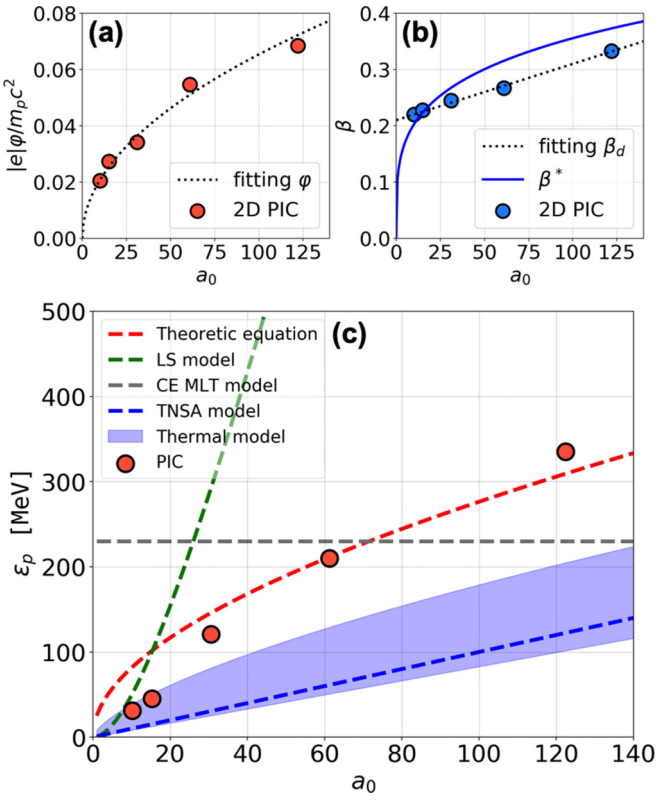

FIG. 8. (a) The electric potential φ extracted from 2D PIC simulations and the dotted black line refers to the fitting $\varphi(a_0)$. (b) Drifting velocity β_d extracted from simulations and the dotted black line marks the fitting β_d while the blue solid line $\beta^*(\varphi)$ is based on the fitting $\varphi(a_0)$. Panel (c) illustrates dependence of the proton cutoff energy on the laser intensity a_0, where the dashed red line corresponds to the theoretical prediction of Eq. (10) while the dashed blue (green) line refers to the scaling of conventional TNSA (LS) model. The blue shadow area represents the model of thermal acceleration with plasma-bound electrons and the gray dashed line denotes the model of Coulomb explosion with mass-limited target.

investigating the proton acceleration via fully self-consistent PIC simulations.

The proton energy spectral for three cases in Fig. 7(a) manifest the plateau-type energy spectrum in the tightly focused condition of $\sigma_0 = 1\ \mu$m and $2\ \mu$m. When calculating the spectral in Fig. 7(a), we collect the protons within a transverse region of $-2 \leqslant y\,[\mu\text{m}] \leqslant 2$ to exclude the peripheral energetic protons induced by the normal sheath field acceleration. The feature of plateau-type energy spectrum is a representative feature of proton sheet crossing, which corresponds well with the theoretical model of Fig. 2 in Sec. II. To further clarify the influence of sheet crossing on proton energy spectral, we show the ratio of the number of protons with different original position to the whole number of protons in each energy bin in Figs. 7(b), 7(c), and 7(d). For simplicity, the protons are divided into three groups based on their initial position. Specifically, the protons with $0.0 \leqslant x\,[\mu\text{m}] < 0.1$ at time $t = 0$ fs are labeled by "left" group. The "mid" and "right" groups correspond the protons with initial position of $0.1 \leqslant x\,[\mu\text{m}] < 0.2$ and $0.2 \leqslant x\,[\mu\text{m}] \leqslant 0.3$, respectively. In the tightly focused cases of Figs. 7(c) and 7(d), the most energetic part are predominantly contributed by the blue "left" protons because the "left" protons tend to be faster than the "right" protons after the occurrence of sheet crossing as shown in Figs. 2(a) and 5(f). However, for the case of large spot size $\sigma_0 = 8\ \mu$m in Fig. 7(b), the most energetic part are exclusively from "right" protons and there is no plateau-type property in its energy spectrum. The reason is that the QSLEF at the front surface of target is no longer greater than the normal sheath electric field at the rear surface. Therefore, the protons do not perform the sheet crossing process in the wide focus situation.

The PIC simulation results indicate that many complex procedures such as relativistic transparency, energy enhancement of hot electrons, and proton sheet crossing are involved in the energy transformation from laser pulse to the energetic proton beams. Here, the values of $\varphi(\xi_0)$ and β_d, which are necessary for the theoretical estimations of Eqs. (8)–(10), are extracted from simulations. The advantage of direct extracting $\varphi(\xi_0)$ and β_d from simulations is more authentic to present the realistic interaction because the PIC simulation has already self-consistently accounted for the whole complicated nonlinear processes. In Fig. 8(a), the red circles denote the electric potential $\varphi(\xi_0)$ of the QSLEF obtained from 2D PIC simulations while the dotted black line refers to the fitting relation $\varphi|_{\xi=\xi_0}(a_0) = 12a_0^{1/2}m_ec^2/|e|$. For simplicity, we utilize φ to represent $\varphi(\xi_0)$ in below text. Based on the fitting $\varphi(a_0)$ and Eq. (9), the criterion of drift velocity for proton sheet crossing occurring can be estimated as $\beta^*(a_0) = \sqrt{1.3\times10^{-2}\sqrt{a_0} - 3.6\times10^{-6}a_0}$, which is shown as solid blue line in the Fig. 8(b). For comparison, the results of β_d extracted from simulations (blue circles) are exhibited as well. The fitting drift velocity $\beta_d = 10^{-3}a_0 + 0.21$ would intersect with $\beta^*(a_0)$ at $a_0^* \approx 15.5$, which indicates that the condition of emerging proton sheet crossing is $a_0 > a_0^*$. The threshold of $a_0^* \approx 16$ is in reasonable agreement with our simulation results in Figs. 7(b)–7(d).

The dependence of proton cutoff energy ε_p on laser field strength a_0 is drawn in Fig. 8(c), where the red circles denote the results from 2D PIC simulation while the dashed red line illustrates the theoretically derived maximum energy of Eq. (10) by utilizing the fitting relation of $\varphi(a_0) = 12a_0^{1/2}m_ec^2/|e|$. The relatively large discrepancy between the theoretical prediction and the PIC simulation results at $a_0 = 10$ and 15 could be understood as that the drift QSLEF is too fast to trap the protons and consequently the drift QSLEF cannot efficiently accelerate them to the high energy plateau under $a_0 < a_0^*$. The discrepancy for the case of $a_0 = 122$, where the simulation manifests the cutoff energy 335 MeV whilst the theory gives $\varepsilon_p \approx 310$ MeV, could be explained by the extra energy boost from the residue electric charge separation field after the proton undergoes the primary drift QSLEF. Considering the parameters in our PIC simulations is only extended to $a_0 = 122$ and the theoretical prediction is partially obtained via fitting the simulation data, we claim that the limits of applicability of the proton sheet crossing model is $a_0^* < a_0 < 130$ under the total laser power of $P = 1$ PW.

For the purpose of comparing our mechanism with others, we consider two optimized thermal acceleration models, which are the acceleration by thermal strong charge separation field (thermal model) [17] and coulomb explosion mechanism with mass-limited targets (CE MLT) [39]. The thermal model, whose scaling law of maximum proton energy is $\varepsilon_p^{\max} = T_e[e^{\varphi^*}(\varphi^* - 1) + 1]/(e^{\varphi^*} - 1)$, is based on an acceleration process induced by the thermal strong charge separation electric field, where the normalized maximum energy of plasma-bound electrons is $\varphi^* = \varepsilon_e^{\max}/T_e$ and it could be approximated by a fitting relation $\varphi^*_{\text{fit}} = \varepsilon_e^{\max}/T_e \approx 4.8 + 0.8 \ln \mathrm{W_L[J]} \approx 7.5$, where $\mathrm{W_L} \approx 30$J is the laser energy in our simulations. The energy relation of $\varepsilon_p^{\max}$ based on thermal model is illustrated in Fig. 7(e) where the upper (lower) boundary of blue shadow area corresponds the fitting relation of electron temperature $T_e = 2.5a_0^{2/3}m_ec^2$ $(0.25a_0m_ec^2)$ at later (earlier) time $t = 93$ (67) fs. The upper estimation of thermal model agrees well with the simulation results for the condition of relative wide laser spot size and low laser intensity but it underestimates the results for the condition of tight focusing and high laser intensity. In CE MLT regime, a target with transverse size equaling or smaller than the laser spot size is employed to eliminate neutralizing currents from the returning electrons and cold surrounding plasmas. As there is intrinsic difference in the target designment between CE MLT and our regime, the energy scaling of light ions accelerated from the CE MLT model $\varepsilon_i \approx 230\,\mathrm{MeV}\mathcal{Z}_i\sqrt{P/\mathrm{PW}}$ as shown in Fig. 7(e) cannot reproduce the tendency of simulation results. The theoretical prediction of proton energy based on TNSA model is plotted as dashed blue line in Fig. 7(e), where $\varepsilon_p^{\mathrm{TNSA}} \sim \rho a_0 m_e c^2 \propto I_0^{1/2}$ underestimates the achieved proton energy in 2D PIC simulations and the coefficient $\rho \approx 2$ accounts for the multidimensional effect of two-dimensional spatial geometry [96]. The predicted proton energy by the model of optimal LS RPA is illustrated as dashed green line in Fig. 7(e), where the energy scaling is $\varepsilon_{\mathrm{LS}} = m_pc^2\mathcal{F}^2/[2(1 + \mathcal{F})]$ with $\mathcal{F} = 2\pi(\mathcal{Z}/A)(m_e/m_p)(\tau_0 c/\lambda_0)a_0$ [97]. Obviously, the scaling of optimal LS RPA is divergent from the simulation results.

TABLE II. Proton charge for different energy range under the condition of $|\theta| < 30^\circ$ and $|y| < 2\,\mu$m.

a_0	>1 MeV	>10 MeV	>100 MeV	>200 MeV
122.4	0.867 nC	0.642 nC	0.638 nC	0.304 nC
61.2	1.300 nC	1.177 nC	0.483 nC	0.044 nC
30.6	4.340 nC	4.262 nC	0.118 nC	0.000 nC
15.3	3.183 nC	2.256 nC	0.000 nC	0.000 nC
10.2	2.554 nC	1.003 nC	0.000 nC	0.000 nC

Besides, the total charge of proton under the condition of $|\theta| < 30^\circ$ and $|y| < 2\,\mu$m for different energy range is listed in Table II, where the size of the third dimension is assumed as $4\,\mu$m in calculating the weight for each macro-particles. The Table III presenting the proton charge under the condition of $|\theta| < 3^\circ$ and $|y| < 2\,\mu$m manifests that the protons nearby central region are well collimated, where the difference in total charge between the cases of $|\theta| < 3^\circ$ and $|\theta| < 30^\circ$ is inconspicuous.

V. SUMMARY AND DISCUSSION

In conclusion, we have identified and characterized the novel phenomenon of proton sheet crossing in acceleration process driven by a drifting self-generated QSLEF. Through theoretical analyses of Hamiltonian dynamics, we clarify that the effectively accelerated ions are first trapped by the potential well of a conserved Hamiltonian $\mathcal{H}$ and then reflected to an enhanced momentum p^r which corresponds to a velocity greater than the drifting velocity v_d of QSLEF. The sheet crossing is an intrinsic feature when the protons are imposed to QSLEF with a longitudinal gradient and the plateau-type energy spectrum generally accompanies with the occurrence of proton sheet crossing. By performing 2D PIC simulations, we examine the scenario of a thin target irradiated by a LP short pulse with power of 1PW under the condition of $\zeta \sim a_0$. Instead of continuously pushing the whole foil moving forward, the laser pulse easily propagates through the classical overdense plasma, where the electrons are effectively heated to a temperature of multi MeVs enabling the occurrence of relativistic transparency. The properties of proton sheet crossing and plateau-type energy spectrum have also been testified in the 2D PIC simulations. It is worth pointing out that a systematic theoretical model and multidimensional PIC simulations are still required to determine which parameters could lead to the occurrence of sheet crossing. In addition, the varying drift velocity of QSLEF with respect to time,

TABLE III. Proton charge for different energy range under the condition of $|\theta| < 3^\circ$ and $|y| < 2\,\mu$m.

a_0	>1 MeV	>10 MeV	>100 MeV	>200 MeV
122.4	0.505 nC	0.465 nC	0.464 nC	0.241 nC
61.2	0.752 nC	0.752 nC	0.344 nC	0.032 nC
30.6	2.645 nC	2.621 nC	0.086 nC	0.000 nC
15.3	3.123 nC	2.255 nC	0.000 nC	0.000 nC
10.2	2.534 nC	1.003 nC	0.000 nC	0.000 nC

i.e., $\partial\beta_d(t)/\partial t \neq 0$, would lead to more complicated sheet crossing processes. The detailed investigation about these several points are beyond the scope of current work and will be performed in the future work.

Nowadays, we are embracing the era of multi-PW laser facilities coming up [98–101]. The high-intensity facilities, such as Bella [102], Vulcan [103], Apollon [104], Texas PW [105], CoReLS [106], etc., have already demonstrated operation at or beyond 1 PW. Via tight focus, the laser intensities to target can reach 10^{22} W/cm^2 while sustaining an ultrahigh contrast like 10^{12} up to 150 ps before the main pulse [106]. The assumption of free of preplasma is valid in the above PIC simulations where the thin foil is directly irradiated by the main pulse. Therefore, the current experimental condition is satisfactory to trigger the occurrence of ion sheet crossing and obtain the boosted protons with energy extending to several hundreds of MeV. Since the most energetic protons originate from the front surface of target as shown in proton energy spectral, it is feasible to come up with a design of enhancing the energetic proton charge through tailoring the plasma target, e.g., adding extra hydrogen coatings. It should be noticed that the spatial geometry of two dimension simulations might suppresses thermal electron diffusion in the transverse direction, leading to an overestimation of the QSLEF, as the electron cloud's spreading is suppressed. Additional three-dimensional simulations are required to confirm whether the predicted ion energies can be actually achieved and the energy flux of ions is superior among other mechanisms [107] in practical circumstances, which beyond the scope of our current work. Here, we humbly claim that our understanding of acceleration dynamics in a QSLEF of the relativistic plasma is potentially beneficial and instructive for the future study on laser-driven ion acceleration.

ACKNOWLEDGMENTS

This work has been supported by Natural Science Foundation of China (Grants No. 11921006 and No. 11535001) and National Grand Instrument Project No. SQ2019YFF010006. The work done by W.M. is supported by NSFC innovation group Project No. 11921006, National Grand Instrument Project No. 2019YFF01014402, and Natural Science Foundation of China (Grant No. 11775010). The PIC code EPOCH was in part funded by the United Kingdom EPSRC Grants No. EP/G054950/1, No. EP/G056803/1, No. EP/G055165/1, and No. EP/M022463/1. The simulations are supported by High-performance Computing Platform of Peking University.

[1] A. Maksimchuk, S. Gu, K. Flippo, D. Umstadter, and V. Y. Bychenkov, Phys. Rev. Lett. **84**, 4108 (2000).
[2] E. L. Clark, K. Krushelnick, J. R. Davies, M. Zepf, M. Tatarakis, F. N. Beg, A. Machacek, P. A. Norreys, M. I. K. Santala, I. Watts, and A. E. Dangor, Phys. Rev. Lett. **84**, 670 (2000).
[3] R. A. Snavely, M. H. Key, S. P. Hatchett, T. E. Cowan, M. Roth, T. W. Phillips, M. A. Stoyer, E. A. Henry, T. C. Sangster, M. S. Singh *et al.*, Phys. Rev. Lett. **85**, 2945 (2000).
[4] H. Daido, M. Nishiuchi, and A. S. Pirozhkov, Rep. Progr. Phys. **75**, 056401 (2012).
[5] A. Macchi, M. Borghesi, and M. Passoni, Rev. Mod. Phys. **85**, 751 (2013).
[6] M. H. Key, Phys. Plasmas **14**, 055502 (2007).
[7] J. C. Fernández, J. Honrubia, B. J. Albright, K. A. Flippo, D. C. Gautier, B. M. Hegelich, M. J. Schmitt, M. Temporal, and L. Yin, Nucl. Fusion **49**, 065004 (2009).
[8] Z. Li, Z. Wang, R. Xu, J. Yang, F. Ye, Y. Chu, Z. Xu, F. Chen, S. Meng, J. Qi *et al.*, Matter Radiat. Extremes **4**, 046201 (2019).
[9] P. Patel, A. Mackinnon, M. Key, T. Cowan, M. Foord, M. Allen, D. Price, H. Ruhl, P. Springer, and R. Stephens, Phys. Rev. Lett. **91**, 125004 (2003).
[10] C. Deutsch and G. Maynard, Matter Radiat. Extremes **1**, 277 (2016).
[11] M. Borghesi, D. Campbell, A. Schiavi, M. Haines, O. Willi, A. MacKinnon, P. Patel, L. Gizzi, M. Galimberti, R. Clarke *et al.*, Phys. Plasmas **9**, 2214 (2002).
[12] U. Linz and J. Alonso, Phys. Rev. ST Accel. Beams **10**, 094801 (2007).
[13] D. Strickland and G. Mourou, Opt. Commun. **55**, 447 (1985).
[14] G. A. Mourou, T. Tajima, and S. V. Bulanov, Rev. Mod. Phys. **78**, 309 (2006).
[15] A. Pukhov, Phys. Rev. Lett. **86**, 3562 (2001).
[16] P. Mora, Phys. Rev. Lett. **90**, 185002 (2003).
[17] M. Passoni, L. Bertagna, and A. Zani, New J. Phys. **12**, 045012 (2010).
[18] A. Pukhov and J. Meyer-ter-Vehn, Phys. Rev. Lett. **79**, 2686 (1997).
[19] X. Zhang, B. Shen, X. Li, Z. Jin, F. Wang, and M. Wen, Phys. Plasmas **14**, 123108 (2007).
[20] X. Zhang, B. Shen, X. Li, Z. Jin, and F. Wang, Phys. Plasmas **14**, 073101 (2007).
[21] F. Pegoraro and S. V. Bulanov, Phys. Rev. Lett. **99**, 065002 (2007).
[22] A. Robinson, P. Gibbon, M. Zepf, S. Kar, R. Evans, and C. Bellei, Plasma Phys. Control. Fusion **51**, 024004 (2009).
[23] N. Naumova, T. Schlegel, V. T. Tikhonchuk, C. Labaune, I. V. Sokolov, and G. Mourou, Phys. Rev. Lett. **102**, 025002 (2009).
[24] T. Esirkepov, M. Borghesi, S. V. Bulanov, G. Mourou, and T. Tajima, Phys. Rev. Lett. **92**, 175003 (2004).
[25] A. Macchi, F. Cattani, T. V. Liseykina, and F. Cornolti, Phys. Rev. Lett. **94**, 165003 (2005).
[26] A. Robinson, M. Zepf, S. Kar, R. Evans, and C. Bellei, New J. Phys. **10**, 013021 (2008).
[27] O. Klimo, J. Psikal, J. Limpouch, and V. Tikhonchuk, Phys. Rev. ST Accel. Beams **11**, 031301 (2008).
[28] X. Q. Yan, C. Lin, Z. M. Sheng, Z. Y. Guo, B. C. Liu, Y. R. Lu, J. X. Fang, J. E. Chen, Phys. Rev. Lett. **100**, 135003 (2008).
[29] B. Qiao, M. Zepf, M. Borghesi, and M. Geissler, Phys. Rev. Lett. **102**, 145002 (2009).

[30] M. Chen, A. Pukhov, T. P. Yu, and Z. M. Sheng, Phys. Rev. Lett. **103**, 024801 (2009).

[31] A. Macchi, S. Veghini, and F. Pegoraro, Phys. Rev. Lett. **103**, 085003 (2009).

[32] L. O. Silva, M. Marti, J. R. Davies, R. A. Fonseca, C. Ren, F. S. Tsung, and W. B. Mori, Phys. Rev. Lett. **92**, 015002 (2004).

[33] M. Chen, Z.-M. Sheng, Q.-L. Dong, M.-Q. He, S.-M. Weng, Y.-T. Li, and J. Zhang, Phys. Plasmas **14**, 113106 (2007).

[34] F. Fiuza, A. Stockem, E. Boella, R. A. Fonseca, L. O. Silva, D. Haberberger, S. Tochitsky, C. Gong, W. B. Mori, and C. Joshi, Phys. Rev. Lett. **109**, 215001 (2012).

[35] L. Yin, B. Albright, B. Hegelich, K. J. Bowers, K. Flippo, T. Kwan, and J. Fernández, Phys. Plasmas **14**, 056706 (2007).

[36] L. Yin, B. J. Albright, K. J. Bowers, D. Jung, J. C. Fernández, and B. M. Hegelich, Phys. Rev. Lett. **107**, 045003 (2011).

[37] T. Nakamura, S. V. Bulanov, T. Z. Esirkepov, and M. Kando, Phys. Rev. Lett. **105**, 135002 (2010).

[38] S. S. Bulanov, V. Y. Bychenkov, V. Chvykov, G. Kalinchenko, D. W. Litzenberg, T. Matsuoka, A. G. Thomas, L. Willingale, V. Yanovsky, K. Krushelnick *et al.*, Phys. Plasmas **17**, 043105 (2010).

[39] T. Z. Esirkepov, S. V. Bulanov, K. Nishihara, T. Tajima, F. Pegoraro, V. S. Khoroshkov, K. Mima, H. Daido, Y. Kato, Y. Kitagawa *et al.*, Phys. Rev. Lett. **89**, 175003 (2002).

[40] S. S. Bulanov, A. Brantov, V. Y. Bychenkov, V. Chvykov, G. Kalinchenko, T. Matsuoka, P. Rousseau, S. Reed, V. Yanovsky, D. W. Litzenberg *et al.*, Phys. Rev. E **78**, 026412 (2008).

[41] T.-P. Yu, A. Pukhov, G. Shvets, and M. Chen, Phys. Rev. Lett. **105**, 065002 (2010).

[42] X. F. Shen, B. Qiao, H. Zhang, S. Kar, C. T. Zhou, H. X. Chang, M. Borghesi, and X. T. He, Phys. Rev. Lett. **118**, 204802 (2017).

[43] B. J. Galow, Y. I. Salamin, T. V. Liseykina, Z. Harman, and C. H. Keitel, Phys. Rev. Lett. **107**, 185002 (2011).

[44] F. Mackenroth, A. Gonoskov, and M. Marklund, Phys. Rev. Lett. **117**, 104801 (2016).

[45] A. Arefiev, T. Toncian, and G. Fiksel, New J. Phys. **18**, 105011 (2016).

[46] H. Cheng, L. Cao, J. Gong, R. Xie, C. Zheng, and Z. Liu, Laser Part. Beams **37**, 217 (2019).

[47] T. Esirkepov, M. Yamagiwa, and T. Tajima, Phys. Rev. Lett. **96**, 105001 (2006).

[48] S. C. Wilks, W. L. Kruer, M. Tabak, and A. B. Langdon, Phys. Rev. Lett. **69**, 1383 (1992).

[49] X. Q. Yan, H. C. Wu, Z. M. Sheng, J. E. Chen, and J. Meyer-ter-Vehn, Phys. Rev. Lett. **103**, 135001 (2009).

[50] B. Qiao, M. Zepf, M. Borghesi, B. Dromey, M. Geissler, A. Karmakar, and P. Gibbon, Phys. Rev. Lett. **105**, 155002 (2010).

[51] M. Kaluza, J. Schreiber, M. I. K. Santala, G. D. Tsakiris, K. Eidmann, J. Meyer-ter-Vehn, and K. J. Witte, Phys. Rev. Lett. **93**, 045003 (2004).

[52] P. McKenna, D. Carroll, O. Lundh, F. Nürnberg, K. Markey, S. Bandyopadhyay, D. Batani, R. Evans, R. Jafer, S. Kar *et al.*, Laser Part. Beams **26**, 591 (2008).

[53] Q. Liao, M. Wu, Z. Gong, Y. Geng, X. Xu, D. Li, Y. Shou, J. Zhu, C. Li, M. Yang *et al.*, Phys. Plasmas **25**, 063109 (2018).

[54] S. Zhang, J. Yu, Y. Shou, Z. Gong, D. Li, Y. Geng, W. Wang, X. Yan, and C. Lin, Phys. Plasmas **27**, 023101 (2020).

[55] A. Sgattoni, S. Sinigardi, L. Fedeli, F. Pegoraro, and A. Macchi, Phys. Rev. E **91**, 013106 (2015).

[56] Y. Wan, C.-H. Pai, C. J. Zhang, F. Li, Y. P. Wu, J. F. Hua, W. Lu, Y. Q. Gu, L. O. Silva, C. Joshi, and W. B. Mori, Phys. Rev. Lett. **117**, 234801 (2016).

[57] A. Higginson, R. Gray, M. King, R. Dance, S. Williamson, N. Butler, R. Wilson, R. Capdessus, C. Armstrong, J. Green *et al.*, Nat. Commun. **9**, 724 (2018).

[58] B. Gonzalez-Izquierdo, M. King, R. J. Gray, R. Wilson, R. J. Dance, H. Powell, D. A. Maclellan, J. McCreadie, N. M. Butler, S. Hawkes *et al.*, Nat. Commun. **7**, 12891 (2016).

[59] A. Henig, S. Steinke, M. Schnürer, T. Sokollik, R. Hörlein, D. Kiefer, D. Jung, J. Schreiber, B. M. Hegelich, X. Q. Yan *et al.*, Phys. Rev. Lett. **103**, 245003 (2009).

[60] J. H. Bin, W. J. Ma, H. Y. Wang, M. J. V. Streeter, C. Kreuzer, D. Kiefer, M. Yeung, S. Cousens, P. S. Foster, B. Dromey *et al.*, Phys. Rev. Lett. **115**, 064801 (2015).

[61] C. Scullion, D. Doria, L. Romagnani, A. Sgattoni, K. Naughton, D. R. Symes, P. McKenna, A. Macchi, M. Zepf, S. Kar, and M. Borghesi, Phys. Rev. Lett. **119**, 054801 (2017).

[62] I. J. Kim, K. H. Pae, I. W. Choi, C.-L. Lee, H. T. Kim, H. Singhal, J. H. Sung, S. K. Lee, H. W. Lee, P. V. Nickles *et al.*, Phys. Plasmas **23**, 070701 (2016).

[63] H. Zhang, B. F. Shen, W. P. Wang, S. H. Zhai, S. S. Li, X. M. Lu, J. F. Li, R. J. Xu, X. L. Wang, X. Y. Liang *et al.*, Phys. Rev. Lett. **119**, 164801 (2017).

[64] T. Toncian, M. Borghesi, J. Fuchs, E. d'Humières, P. Antici, P. Audebert, E. Brambrink, C. A. Cecchetti, A. Pipahl, L. Romagnani *et al.*, Science **312**, 410 (2006).

[65] L. Willingale, S. R. Nagel, A. G. R. Thomas, C. Bellei, R. J. Clarke, A. E. Dangor, R. Heathcote, M. C. Kaluza, C. Kamperidis, S. Kneip *et al.*, Phys. Rev. Lett. **102**, 125002 (2009).

[66] D. Haberberger, S. Tochitsky, F. Fiuza, C. Gong, R. A. Fonseca, L. O. Silva, W. B. Mori, and C. Joshi, Nat. Phys. **8**, 95 (2012).

[67] S. Palaniyappan, C. Huang, D. C. Gautier, C. E. Hamilton, M. A. Santiago, C. Kreuzer, A. B. Sefkow, R. C. Shah, and J. C. Fernández, Nat. Commun. **6**, 10170 (2015).

[68] J. Braenzel, A. A. Andreev, K. Platonov, M. Klingsporn, L. Ehrentraut, W. Sandner, and M. Schnürer, Phys. Rev. Lett. **114**, 124801 (2015).

[69] M. H. Helle, D. F. Gordon, D. Kaganovich, Y. Chen, J. P. Palastro, and A. Ting, Phys. Rev. Lett. **117**, 165001 (2016).

[70] J. H. Bin, M. Yeung, Z. Gong, H. Y. Wang, C. Kreuzer, M. L. Zhou, M. J. V. Streeter, P. S. Foster, S. Cousens, B. Dromey *et al.*, Phys. Rev. Lett. **120**, 074801 (2018).

[71] S. Gaillard, T. Kluge, K. Flippo, M. Bussmann, B. Gall, T. Lockard, M. Geissel, D. Offermann, M. Schollmeier, Y. Sentoku *et al.*, Phys. Plasmas **18**, 056710 (2011).

[72] F. Wagner, O. Deppert, C. Brabetz, P. Fiala, A. Kleinschmidt, P. Poth, V. A. Schanz, A. Tebartz, B. Zielbauer, M. Roth *et al.*, Phys. Rev. Lett. **116**, 205002 (2016).

[73] W. J. Ma, I. J. Kim, J. Q. Yu, I. W. Choi, P. K. Singh, H. W. Lee, J. H. Sung, S. K. Lee, C. Lin, Q. Liao *et al.*, Phys. Rev. Lett. **122**, 014803 (2019).

[74] S. Bulanov, T. Z. Esirkepov, Y. Hayashi, M. Kando, H. Kiriyama, J. Koga, K. Kondo, H. Kotaki, A. Pirozhkov, S. Bulanov *et al.*, Nucl. Instrum. Methods Phys. Res., Sect. A **660**, 31 (2011).

[75] A. Di Piazza, C. Müller, K. Z. Hatsagortsyan, and C. H. Keitel, Rev. Mod. Phys. **84**, 1177 (2012).
[76] E. Esarey and M. Pilloff, Phys. Plasmas **2**, 1432 (1995).
[77] B. Liu, J. Meyer-ter Vehn, K. Bamberg, W. Ma, J. Liu, X. He, X. Yan, and H. Ruhl, Phys. Rev. Accelerat. Beams **19**, 073401 (2016).
[78] B. Shen, Y. Li, M. Y. Yu, and J. Cary, Phys. Rev. E **76**, 055402(R) (2007).
[79] S. Weng, M. Murakami, P. Mulser, and Z. Sheng, New J. Phys. **14**, 063026 (2012).
[80] L. Ji, B. Shen, X. Zhang, F. Wang, Z. Jin, X. Li, M. Wen, and J. R. Cary, Phys. Rev. Lett. **101**, 164802 (2008).
[81] W. Zhang, B. Qiao, T. Huang, X. Shen, W. You, X. Yan, S. Wu, C. Zhou, and X. He, Phys. Plasmas **23**, 073118 (2016).
[82] H. B. Zhuo, Z. L. Chen, W. Yu, Z. M. Sheng, M. Y. Yu, Z. Jin, and R. Kodama, Phys. Rev. Lett. **105**, 065003 (2010).
[83] T. Arber, K. Bennett, C. Brady, A. Lawrence-Douglas, M. Ramsay, N. Sircombe, P. Gillies, R. Evans, H. Schmitz, A. Bell *et al.*, Plasma Phys. Control. Fusion **57**, 113001 (2015).
[84] P. Gibbon, *Short Pulse Laser Interactions with Matter* (World Scientific, Singapore, 2004).
[85] T. Tajima and J. M. Dawson, Phys. Rev. Lett. **43**, 267 (1979).
[86] R. Hu, Z. Gong, J. Yu, Y. Shou, M. Lv, Z. Sheng, T. Tajima, and X. Yan, Int. J. Mod. Phys. A **34**, 1943012 (2019).
[87] See Supplemental Material at http://link.aps.org/supplemental/10.1103/PhysRevE.102.013207 for the animation of charged particle motion.
[88] A. Pukhov and J. Meyer- ter-Vehn, Phys. Rev. Lett. **76**, 3975 (1996).
[89] A. Pukhov, Rep. Prog. Phys. **65**, 1 (2002).
[90] A. Pukhov, Z.-M. Sheng, and J. Meyer-ter Vehn, Phys. Plasmas **6**, 2847 (1999).
[91] J. Meyer-ter Vehn and Z. M. Sheng, Phys. Plasmas **6**, 641 (1999).
[92] A. Sorokovikova, A. V. Arefiev, C. McGuffey, B. Qiao, A. P. L. Robinson, M. S. Wei, H. S. McLean, and F. N. Beg, Phys. Rev. Lett. **116**, 155001 (2016).
[93] A. Arefiev, V. Khudik, A. Robinson, G. Shvets, L. Willingale, and M. Schollmeier, Phys. Plasmas **23**, 056704 (2016).
[94] T. Huang, C. Zhou, A. Robinson, B. Qiao, A. Arefiev, P. Norreys, X. He, and S. Ruan, Phys. Plasmas **24**, 043105 (2017).
[95] Z. Gong, A. Robinson, X. Yan, and A. Arefiev, Plasma Phys. Control. Fusion **61**, 035012 (2019).
[96] K. Xiao, C. Zhou, K. Jiang, Y. Yang, R. Li, H. Zhang, B. Qiao, T. Huang, J. Cao, T. Cai *et al.*, Phys. Plasmas **25**, 023103 (2018).
[97] A. Macchi, C. Livi, and A. Sgattoni, J. Instrument. **12**, C04016 (2017).
[98] C. Danson, D. Hillier, N. Hopps, and D. Neely, High Power Laser Sci. Eng. **3**, e3 (2015).
[99] C. N. Danson, C. Haefner, J. Bromage, T. Butcher, J.-C. F. Chanteloup, E. A. Chowdhury, A. Galvanauskas, L. A. Gizzi, J. Hein, D. I. Hillier *et al.*, High Power Laser Sci. Eng. **7**, e54 (2019).
[100] Y.-J. Gu, M. Jirka, O. Klimo, and S. Weber, Matter Radiat Extremes **4**, 064403 (2019).
[101] Z. Gong, R. Hu, Y. Shou, B. Qiao, C. Chen, F. Xu, X. He, and X. Yan, Matter Radiat Extremes **1**, 308 (2018).
[102] W. P. Leemans, R. Duarte, E. Esarey, S. Fournier, C. G. R. Geddes, D. Lockhart, C. B. Schroeder, C. Toth, J. Vay, and S. Zimmermann, in *Advanced Accelerator Concepts: 14th Advanced Accelerator Concepts Workshop*, edited by S. H. Gold and G. S. Nusinovich, AIP Conf. Proc. No. 1299 (AIP, New York, 2010).
[103] C. Danson, P. Brummitt, R. Clarke, J. Collier, B. Fell, A. Frackiewicz, S. Hancock, S. Hawkes, C. Hernandez-Gomez, P. Holligan *et al.*, Nucl. Fusion **44**, S239 (2004).
[104] J. Zou, C. Le Blanc, D. Papadopoulos, G. Chériaux, P. Georges, G. Mennerat, F. Druon, L. Lecherbourg, A. Pellegrina, and P. Ramirez, High Power Laser Sci. Eng. **3**, e2 (2015).
[105] E. W. Gaul, M. Martinez, J. Blakeney, A. Jochmann, M. Ringuette, D. Hammond, T. Borger, R. Escamilla, S. Douglas, W. Henderson *et al.*, Appl. Opt. **49**, 1676 (2010).
[106] J. W. Yoon, C. Jeon, J. Shin, S. K. Lee, H. W. Lee, I. W. Choi, H. T. Kim, J. H. Sung, and C. H. Nam, Opt. Express **27**, 20412 (2019).
[107] F. Mackenroth, A. Gonoskov, and M. Marklund, Eur. Phys. J. D **71**, 204 (2017).